Morphology of Integral-Skin Layers in Hollow-Fiber Gas-Separation Membranes

Seth B. Carruthers,* Gabriela L. Ramos,† William J. Koros

School of Chemical Engineering, Georgia Institute of Technology, Atlanta, Georgia 30332-0100

Received 7 October 2002; accepted 13 January 2003

ABSTRACT: The morphologies of polymeric integrally skinned asymmetric gas-separation membranes are typically visualized as a thin gas-selective skin region supported by a nonselective, low-resistance porous structure. The validity of this visualization for defect-free *and* defective membranes was investigated via scanning electron microscopy (SEM) in combination with traditional gas-permeation measurements for previously reported ultrathin defect-free hollow-fiber membranes. Hollow-fiber membranes were formed via a dry-jet, wet-quench process with a spinning solution composed of Matrimid® polyimide and components of varying volatility. For all the *defect-free* membranes formed, SEM images revealed a prominent dense skin layer across the fibers' entire outer circumference. Skin-thickness estimates from 36 SEM images and N_2, O_2, and He pure gas-permeation measurements agreed to within 9, 7, and 24% for defect-free membranes with 150-, 300-, and 600-nm skin thicknesses, respectively. *Defective* membranes with O_2/N_2 gas selectivities of Knudsen values, nominally 50 and 80% of dense film values, exhibited a well-developed nodular, partially developed nodular, and uniform dense layer (no nodules) skin morphologies, respectively. These results provide in-depth experimental evidence for the existence of a distinct dense integral-skin layer and suggest that the presence of nodules in the membrane's final skin morphology correlate to gas-permeation defects. © 2003 Wiley Periodicals, Inc. J Appl Polym Sci 90: 399–411, 2003

Key words: membranes; gas permeation; polyimides; fibers

INTRODUCTION

The gas selectivity of polymeric asymmetric gas-separation membranes is attributed to a minute and often difficult-to-define skin layer. Typical gas-separation hollow-fiber membranes have an o.d. of 200 μm and a skin thickness of 100 nm. In other words, over 99% of the hollow-fiber membrane is simply a nonselective porous support, while the remaining <1% governs the membrane's permeation properties. Thus, control of the skin layer is critical as membrane manufacturers strive to form the thinnest skin possible without creating defects or pores. Indeed, pores of ~5 Å wide in the skin layer exceeding area fractions of one in 1 million will render the entire membrane ineffective.[1,2]

The skin layer's gas selectivity may be classified as either "defect-free" or "defective." A skin is conventionally taken to be defect-free if its selectivity for a given gas pair is ≥90% of the polymer's intrinsic dense film value.[3] The morphology of a defect-free skin is typically visualized as a nonporous isotropic polymer film, and permeation is considered to be solely governed by solution–diffusion. The thickness of a defect-free skin layer may be estimated from the asymmetric membrane's permeance and dense film intrinsic permeability values, namely,

$$l_{\text{skin}} = \frac{\mathbf{P}_A^{(\text{dense film})}}{(\mathbf{P}/l)_{A\ (\text{asymmetric membrane})}} \quad (1)$$

Practically speaking, defective selectivities may range from values <90% of dense film values to values equal to Knudsen selectivities. In extreme cases, of course, with viscous flow dominating, no molecular discrimination is possible; however, all the membranes discussed here have at least Knudsen selectivities. Gas permeation may be governed by a combination of solution–diffusion, Knudsen diffusion, and viscous flow. The morphology of defective skin layers is still not well understood, yet may be assumed to have traversing pinhole defects or connected regions of lower polymer density through the skin layer. The nonequilibrium nature of glassy polymers can make even pore-free, rapidly quenched skin layers show lower selectivity than that of a slowly formed thick, dense film sample of a given glassy polymer. There is little agreement on skin-layer morphologies, and these classifications should be considered general reference points and not absolute boundaries.[4–6]

In dry-jet/wet-quench fiber spinning, the skin layer is formed as an integral part of the porous substruc-

Correspondence to: W. J. Koros.

**Present address:* Intel Corp., Ronler Acres Campus, 2501 NW 229th St. Hillsboro, OR 97124.

†*Present address:* Henry M Jackson Foundation, 1600 E Gude, Rockville, MD 20850.

Contract grant sponsor: Air Liquide.

Journal of Applied Polymer Science, Vol. 90, 399–411 (2003)

TABLE I
Overview of Defect-free Flat-sheet Membrane Formation and Characterization

			Permeation[a]		SEM[b]		
Senior author	Polymer	Technique	D-Free?	(nm)	#	Morph	Quant
Kawakami[10]	PI	Dry/wet	Yes	25	1	?	No
Kim[11]	PSf	Dual	Yes	6,200	1	D?	No
Kawakami[12]	PI	Dry/wet	Yes	34	3	D	~
Pesek[13]	PSf	Dry/wet	Yes	60	7	D-N?	No
Van't Hof[15]	PESf	Dual	Yes	600	0	—	No
Pinnau[14]	PC . . .	Dry/wet	Yes	30	0	—	No
Pinnau[16,17]	PSf	Dry/wet	Yes	20	≫1	D-N?	No

[a] D-Free? (Yes), membrane gas selectivity ≥90% dense film values; (nm), skin thickness as estimated from permeation data;
[b] #, No. accompanying published SEM images; Morph, apparent morphology of the skin layer; D, dense; D–N, dense–nodular; N, nodular; (?), ambiguous morphology; Quant, quantitative comparison of skin thickness by SEM and gas permeation data; ~, order of magnitude agreement.

ture in the same step and this entire morphology is mostly formed within 1 s. This type of membrane formation has been widely accepted due mainly to its ability to form skin layers an order of magnitude thinner than can competing methods.[4,7] Despite these advantages, thin *defect-free* skin layers (100 nm) have been only recently formed under commercially relevant conditions in research laboratories.[8,9] Essentially all commercial membranes are formed as *defective*, yet ultrathin skinned membranes and rely on a posttreatment process to improve the membrane's selectivity to acceptable levels. Even though these processes are quite prevalent and efficient for modern membrane materials, posttreated ("caulked") defective skin layers might not take full advantage of next-generation membrane materials as well as truly defect-free skin layers. While an expertise is steadily developing for forming defect-free skin layers, characterization techniques remain heavily based on gas-permeation measurements. While the formation and function of the skin layer are being thoroughly investigated, the actual *form* or morphology of the skin layer remains unclear. This article discusses the use of high-resolution SEM analysis as a supporting characterization technique for gas-separation membranes and how this "combinatorial" analysis can clarify the various degrees of skin morphologies.

BACKGROUND

Previous work has shown that defect-free membranes can be formed from polymeric systems employing wet, dry/wet, and dual-bath techniques. Hand-cast *flat-sheet* membranes from polyimides, polysulfones, and polycarbonates have displayed attractive thin defect-free skins.[10–17] However, characterization of these ultrathin skins has proven difficult beyond gas-permeation measurements.

Previously published SEM images have been somewhat ambiguous while portraying the skin as a collection of nodules, a dense layer, or a blend of the two morphologies. Quantitative estimates of the skin layer's thickness have not been possible and any further interpretation of the skin morphology has been based on qualitative idealized arguments.[6,18–21] Nevertheless, these previous SEM images have been helpful in showing a general asymmetry in the membrane's outer morphology. Table I gives a summary of key articles dealing with the formation and characterization of prevalent defect-free flat-sheet membranes. While flat-sheet formation studies have given valuable insight into the principles of membrane and skin-layer formation, *hollow-fiber* formation is typically best suited for commercial mass production of gas-separation membranes.

Hollow-fiber spinning introduces the new complexities such as short time scales (<1 s), extensional rheology concerns, and simultaneous management of the membrane's self-supporting structure along with its gas-permeation properties. Posttreatment processes have been shown to "repair" defective hollow-fiber membranes and were a landmark contribution to the commercialization of gas-separation membranes. These posttreated membranes can exhibit effectively dense film gas selectivities and ultrathin skin thicknesses. Without posttreatment, the membranes generally display unattractive gas selectivities between Knudsen values and 50% of dense film values.[18,22–35]

Defect-free hollow-fiber membranes have been formed that display >90% of dense film gas selectivities without posttreatment.[15,36–39] However, these membranes generally display substantially thicker skin layers or commercially impractical macroscopic properties and formation conditions. A practical defect-free hollow-fiber membrane would typically have an ultrathin skin on the order of 100 nm, a small outside diameter of less than 300 μm, and a macrovoid-free morphology and allow formation rates of at least 50 m/min.[28,40] The formation of commercially relevant defect-free unposttreated hollow-fiber membranes with thin selective layers and optimized macrovoid-free supports has only recently been shown to

TABLE II
Overview of Prevalent Hollow-fiber Membrane Formation and Characterization

			Permeation[a]		SEM			Commercial[b]		
Senior author	Polymer	Technique	D-Free?	(nm)	#	Morph	Quant	O.d.	MVFree	TkUp
Clausi[8]	PI	Dry/wet	Yes	100				•	•	•
Niwa[36]	PI	Dry/wet	Yes	470	1	D				
Li[37]	PESf . . .	Dual	Yes	300+	1	D				
Pesek[38]	PSf	Dry/wet	Yes	120						
Chung[39]	PI	Wet	Yes	200	1	D?	~		•	
van't Hof[15]	PSf	Dual	Yes	1200	1	D	Yes			
Wang[22]	PSf	Dry/wet	No (pt)	(40+)	1	?				
Chung[23]	PSf	Wet	No (pt)	(130+)	2	D?				
Chung[24]	PESf	Wet	No (pt)	(47)	1	?	~			
Wang[25]	PEI	Dry/wet	No (pt)	(550+)	3	D	~			
Wang[26]	PESf	Dry/wet	No (pt)	(50+)	8	D-N?			•	
Ekiner[27,28]	PA	Dry/wet	No (pt)	(100)	1	D-N?		•	•	•
Fritzsche[18,29–33]	PSf . . .	Dry/wet	No (pt)	(50+)	≫1	D-N	~		•	•
Cabasso[34,35]	PSf	Dry/wet	No	—	1	?		•		•

[a] D-Free?: untreated (Yes) or post-treated [No (pt)] selectivity ≥90% dense film values; (nm), skin-thickness estimate; parentheses, selectivity *after* posttreatment:
[b] Commercially relevant conditions: O.d. (•), outside diameter less than 300 μm; MVFree (•), macrovoid-free morphology; TkUp (•), take-up speed at least 50 m/min.

be possible.[8] Some of the more prevalent work in the formation and characterization of defect-free and defective/posttreatable hollow fibers is summarized in Table II.

Despite these advances in membrane formation, the *morphology* of the skin layer and its subsequent effects on gas permeation remain unclear. The two extremes of the visualization are a severely defective nodular layer and a defect-free dense nonporous skin. However, there remains minimal supporting evidence, seen in Tables I and II, as to the overall morphology of the skin layer or the presence of a unique defect-free skin layer. It is challenging that the most critical element of the membrane, the skin layer, is the least understood. The present work investigated the general visualizations of the skin layer with use of the defect-free hollow-fiber-formation protocol described by Clausi and Koros.[8]

EXPERIMENTAL

Membrane formation

Integrally skinned asymmetric hollow-fiber membranes were formed via a dry-jet/wet-quench spinning process. The specific formation protocols were expanded from those previously reported[8] to form defect-free and defective membranes exhibiting a full spectrum of gas-permeation properties. The polymer dope consisted of the polyimide Matrimid® 5218, 1-methyl-2-pyrrolidinone (NMP, Sigma-Aldrich, St. Louis, MO), tetrahydrofuran (THF, EMD Chemicals, Inc., Gibbstown, NJ), and ethanol (EtOH, AAPER Alcohol & Chemical Co., Shelbyville, KY). The components were obtained from Vantico (Hawthorne, NY); Aldrich (99% grade); EM Science (99.9% grade), and AAPER Alcohol and Chemical Co. (200 proof), respectively. The Matrimid® powder was dried at 120°C under a vacuum overnight and stored in a desiccator until needed. In the dope formulation, NMP was considered the "nonvolatile" solvent, while THF and EtOH were used as a volatile solvent and volatile nonsolvent, respectively. A dope formulation of Matrimid®/NMP/THF/EtOH at 26.2/53.0/5.9/14.9% wt was abbreviated as M3 and used as the control case dope for hollow-fiber formation. Tap water was used as the nonsolvent quench medium. The dehydration procedures employed methanol (MeOH) and *n*-hexanes, which were both used as received from EM Science. The pertinent material properties of Matrimid®

TABLE III
Typical Properties of Matrimid® 5218

α O_2/N_2	α He/N_2	$\mathbf{P}_{N_2}$ (Barrer)	$\mathbf{P}_{O_2}$ (Barrer)	$\mathbf{P}_{He}$ (Barrer)	T_g (°C)	ρ (g/cc)	M_w
7.2	109–113	0.185	1.32–1.35	20.7–22.5	305–315	1.2	86,000

Dense film gas-permeation measurements made at 25°C (ref. 41); T_g from DSC scans at 10°C/min; film density[43] and polymer weight-average molecular weight as determined by GPC with polystyrene standards.[9]

TABLE IV
Typical Properties of Liquids Used During Hollow-fiber Membrane Formation[15,43]

Component	*bp* (°C)	P_{sat} (mmHg)	Surface tension, σ (dynes/cm)	Comment
NMP	202	0.33	40.7 (ref.15)	Solvent
THF	65	142	26.4	Solvent
EtOH	78	44	22.3	Nonsolvent
MeOH	65	97	22.5	Nonsolvent
Acetone	56	184	23.3	Nonsolvent
Hexane	69	124	17.9	Nonsolvent
Water	100	17.5	72.8	Nonsolvent

and the remaining components used during fiber formation are listed in Tables III and IV.

Spin dopes were mixed in 1-L Qorpak® glass bottles sealed with Teflon® caps and dissolved using bottle rotators. The dope can also be mixed in a 2-L sealed Pyrex® reaction vessel with mixing provided by a 1/17-horsepower laboratory stirrer (G. K. Heller, Floral Park, NY). Mild heat (<40°C) was used along with the mechanical mixing to easily dissolve the dopes within 24 h. Once the dope was homogeneous, it was poured into a 500-mL syringe pump (Isco, Model 500D or LC-5000, Lincoln, NE) and allowed to degas for at least 24 h.

A bore fluid mixture of NMP and distilled water was mixed immediately prior to fiber formation and loaded into a separate 500-mL Isco syringe pump. The dope and bore fluid were filtered in-line between the Isco delivery pumps and the spinneret with 100- and 2-μm sintered metal filters, respectively (Nupro Co., Willoughby, OH). Once filtered, the dope and bore fluid were coextruded through a monolithic spinneret on loan from Air Liquide and used by Clausi and Koros.[8] For the control case, the spinneret was heated to 50°C and allowed to equilibrate for 1 h before spinning. Calibrated thermocouples were placed on the spinneret, on the dope filter, and inside the spinneret immersed in the dope stream. All thermocouples were in agreement to ±3°C. The nascent membrane was extruded into an air gap at ambient temperature and 45–67% relative humidity. Once passing through the air gap, the nascent membrane was immersed into a 20-gal water-quench bath held at 25°C. The resulting phase-separated fiber spin line was passed over Teflon® guides within the quench bath and was collected on a 0.32-m-diameter polyethylene drum.[44] The take-up drum was partially immersed in a separate tap water bath during collection to continually wet the hollow fibers.

Once cut off of the take-up drum, the fibers were stored sequentially in at least three separate water baths over the course of 48 h. The fibers were then solvent-exchanged in glass containers with three sequential 20-min MeOH baths followed by three sequential 20-min hexane baths. The fibers were allowed to dry in ambient air for 30 min, then under a vacuum at 120°C for 1 h. The hollow fibers did *not* undergo any coating posttreatment procedures. An overview of the dope composition, spinning conditions, and dehydration procedure for the control case of Matrimid® hollow-fiber membranes is given in Table V.

Membrane characterization

The dried hollow-fiber membranes were potted into double-ended modules made from 50 hollow fibers, with an active membrane length and area of nominally 20 cm and 70 cm^2. Pure gas-permeation measurements were conducted on the modules using N_2, O_2, and He gases all obtained from Air Liquide at 99.999% purity. The gas-permeation measurements were taken at 25°C using a feed gas at nominally 100.0 psig with an ambient permeate pressure. All modules were tested in a bore-fed configuration unless otherwise noted. Three modules were tested for each sample state. Permeate flow rates were determined by 10, 100- or 1000-mL bubble flowmeters. The fibers were allowed to equilibrate over 15 min and rechecked after 45 min to address any fluctuations over time. Duplicate permeation data were taken from three different spin dope batches and hollow-fiber spinning experiments. Variability was observed mainly at relatively small air-gap distances and between different dope batches. The pure gas permeances stabilized quickly to their steady-state values and displayed less than a 5% change over the 45 min of testing.

TABLE V
Formation Conditions for Matrimid® Hollow-fiber Membranes (Control Case)

Dope ("M3")	
Matrimid	26.2% wt.
NMP	53.0
THF	5.9
EtOH (mixed ~24 h ≤ 40°C)	14.9
Sequential dehydration procedure	
(1) Water baths	3–4 (over 3 days)
(2) MeOH baths	3 (20 min each)
(3) Hexane baths	3 (20 min each)
(4) Ambient dry	30 min
(5) 120°C + vacuum	1 h
Spinning conditions	
Dope flow rate	180 mL/h
Bore fluid	60 mL/h, 95/5 (NMP/water)
Spinneret temperature	50°C
Air gap	0.1–40 cm, ambient temperature, 45–65% RH
Quench bath	Tap water, 25°C
Take-up rate	50 m/min
Extrusion pressure	300–400 psig

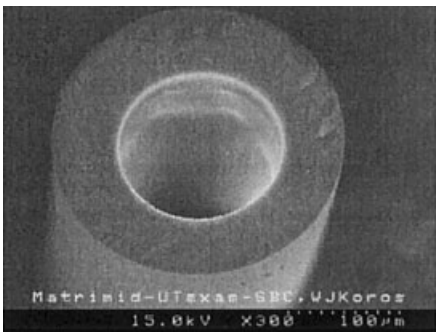

Figure 1 Crosssection of an M3 Matrimid® control-case hollow-fiber membrane.

Fiber cross sections were prepared for SEM analysis by cryofracturing the fiber in liquid N_2 and then sputter coating the cross section with elemental chromium or a gold/palladium alloy. The samples were imaged on a Hitachi S-4500 field-emission SEM (Hitachi, Ltd., Japan) typically using an accelerating voltage of 15 kV, a current of 10 μA, and a working distance of 15 mm. Fiber diameters were measured using a calibrated optical microscope (Leitz, Germany) and verified with SEM.

RESULTS AND DISCUSSION

The M3 Matrimid® dope was easily spinnable and allowed for take-up rates of over 100 m/min, air gap distances of 0.1–40 cm, and spinning temperatures from ambient to over 90°C. The hollow-fiber membranes displayed excellent cross-sectional circularity, and no macrovoids were detected within the fiber wall. The hollow fiber o.d. and i.d. were 230 and 120 μm, respectively, $\pm$10 μm. A typical cross section of the hollow fiber is shown in Figure 1.

The rheological properties of the dope were stable enough to withstand relatively high draw ratios as long as a *minimal* dry step, or air-gap distance, was employed. At air-gap distances less than 0.1 cm, the water-quench bath tended to periodically contact the face of the spinneret and thus eliminate the air gap. During this wet-phase separation (as opposed to dry-jet/wet-quench), the nascent membrane spin line immediately broke. At air-gap distances greater than 40 cm, the freefall velocity of the nascent fiber became greater than the 50 m/min take-up velocity and resulted in the formation of coiled hollow fibers. Therefore, the maximum range of air-gap distances was determined to be from 0.1 to 40 cm. This exceeds the typical range used in most practical spinning processes, so it allowed a thorough investigation of relevant operational conditions.

Gas permeation

The pure gas-permeation data for the unposttreated control case M3 Matrimid® hollow fibers are summarized in Table VI and Figures 2 and 3. Membranes formed using air-gap distances of at least 2 cm displayed defect-free α_{O_2/N_2} and predominately defect-free α_{He/N_2}. The α_{O_2/N_2} ranged from 94 to 105% of the Matrimid® dense film value of 7.2, and the α_{He/N_2} ranged from 80 to 105% of the mean dense film value of 111. The slight depression in He/N_2 selectivities relative to O_2/N_2 selectivities suggests that a small amount of substructure resistance could be present in the membranes. Hollow fibers formed using a 0.1-cm air gap exhibited minimal gas selectivity.

SEM analysis

The macroscopic properties of the hollow fibers were shown to be acceptable by low-magnification SEM images as seen in Figure 1. SEM images at 30,000× were able to characterize a nodular "skin" morphology for the low-selectivity membranes formed using a 0.1-cm air gap. For the defect-free membranes formed using a 2-, 10- and 40-cm air gap, a dense one-phase layer could be seen around the entire circumference of the cross sections. The dense outer layer typically transitioned into a partially developed nodular morphology underneath, which, in turn, led to a more well-developed nodular morphology similar to that found in the 0.1-cm air-gap defective hollow fibers. The dense layer and partially developed nodular region were not present in the defective 0.1-cm air-gap membranes. Example SEMs of defective and defect-free skin morphologies are shown in Figure 4.

The thickness of the outer dense layer for the defect-free membranes increased significantly with the air-

TABLE VI
Pure Gas-permeation Data for the Control-case M3 Matrimid® Hollow Fibers (25°C, Bore-fed)

Air gap (cm)	Selectivity		Permeance (GPU)		
	O_2/N_2	He/N_2	N_2	O_2	He
0.1	2.0	12	16	33	195
2	6.8	109	1.44	9.8	157
2	7.2	99	1.26	9.1	125
2	7.6	110	1.10	8.4	122
6	7.5	115	0.76	5.7	88
6	7.5	96	0.91	6.8	88
10	7.3	102	0.59	4.3	60
10	7.5	117	0.57	4.3	67
10	7.6	118	0.58	4.5	69
10	7.3	112	0.61	4.4	68
10	7.3	95	0.55	4.0	52
10	7.6	99	0.64	4.9	64
10	7.4	101	0.80	5.9	81
10	7.5	96	0.69	5.2	66
10	7.0	92	0.53	3.8	49
10	7.3	97	0.54	3.9	52
40	7.3	106	0.30	2.2	32
40	6.9	101	0.27	1.9	27
40	7.4	100	0.31	2.3	31

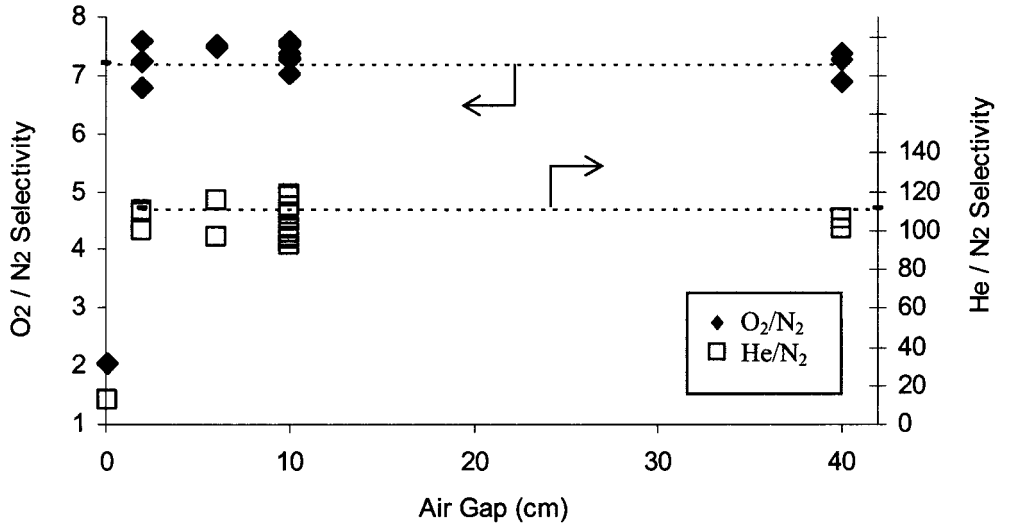

Figure 2 Effect of air-gap distance on the O_2/N_2 and He/N_2 selectivities for the M3 control case Matrimid® hollow fibers at 25°C. The dashed lines represent the dense film values seen in Table III.

gap distance. Images taken at 100,000× were able to semiquantitatively characterize the outer dense layer's thickness. The outer layer's thickness was defined as the distance from the edge of the cross section to the beginning of the compacted nodular layer. Three separate cross sections were taken from each set of hollow fibers formed at 0.1-, 2-, 10- and 40-cm air-gap distances. From each cross section, 12 regions of the outer skin layer were examined around the circumference; thus, a total of 36 dense layer thickness estimates were recorded for each air-gap distance. Typical SEMs of the skin region are displayed in Figure 5.

Defect-free skin-thickness estimates from SEM data were comparable to skin-thickness estimates from pure gas-permeation data. This is the first time such a quantitative relationship has been demonstrated for what has been taken to be a reasonable model of the controlling skin resistance in asymmetric hollow fibers. Effective defect-free skin thicknesses for the 2-, 10- and 40-cm air-gap membranes were calculated using eq. (1), the N_2, O_2, and He permeation measurements in Table VI, and the Matrimid® dense film values in Table III. This calculation is *not* considered valid for the 0.1-cm air-gap hollow fibers since they displayed defective gas selectivities. Skin-thickness estimates from the SEM and gas-permeation data are shown in Figure 6 and Table VII with 95% confidence intervals as determined by

$$\bar{l}_{\text{skin}} \pm t_{(0.05/2,n-1)}\left(\frac{s}{\sqrt{n}}\right) \tag{2}$$

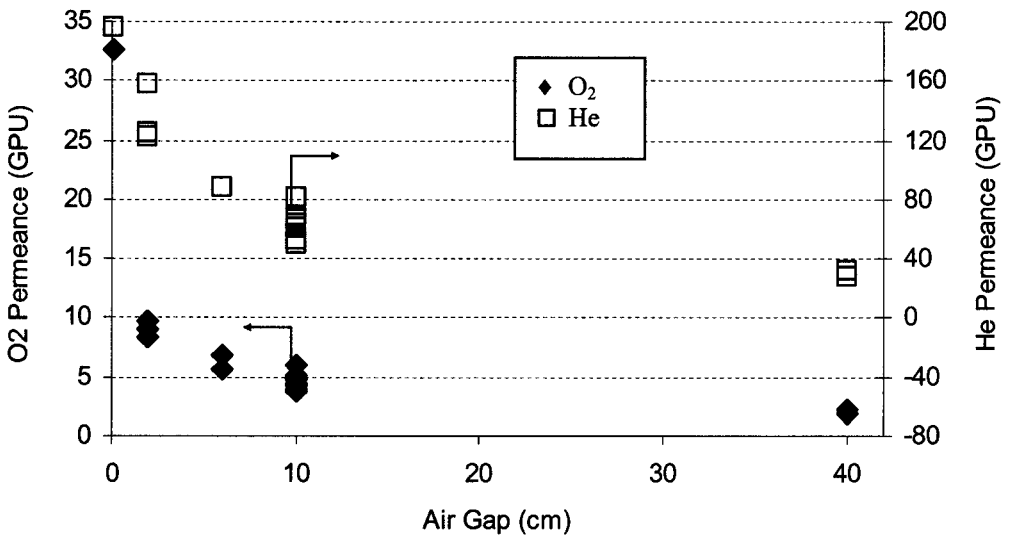

Figure 3 Effect of air-gap distance on the O_2 and He permeances for the control case M3 Matrimid® fibers at 25°C.

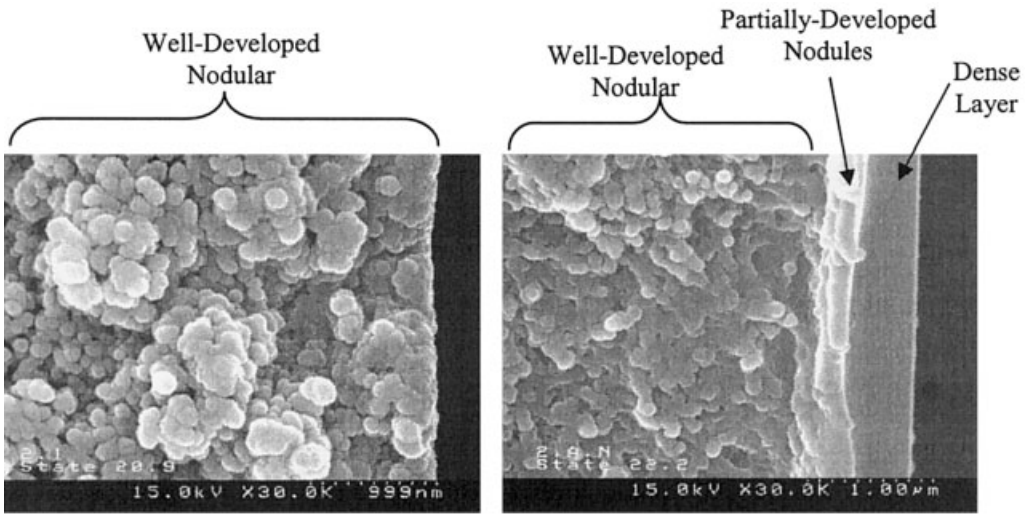

Figure 4 SEM images of the skin region from M3 hollow-fiber membrane crosssections: (a) 0.1-cm air gap, defective gas selectivity; (b) 10-cm air gap, defect-free gas selectivity. ×30 k.

assuming a normal distribution and where $\bar{l}_{skin}$ is the mean estimated skin thickness, $t_{(0.05/2,n-1)}$ is the one-sided t statistic at 95% confidence for $n-1$ degrees of freedom; n, the number of measurements; and s, the sample standard deviation.[45]

The skin-thickness estimates based on SEM and permeation data agreed within experimental error for the hollow fibers formed from 2- and 10-cm air-gap distances. The discrepancy for the thick-skinned membranes formed at 40 cm may be partially due to the difficulty in characterizing the transition layer. The skin thickness was conservatively estimated since the boundary between the dense skin layer and the underlying compacted nodular transition layer is somewhat ambiguous from the SEM images. Thus, the SEM-based skin thickness may be underestimated if the nodular transition layer exhibits significant gas selectivity. Additionally, if the transition layer offers *unselective* resistance, as suggested by the slightly depressed He/N_2 selectivity, the helium permeation data may have overestimated the skin thickness. Nevertheless, there is reasonable agreement between the high-resolution SEM images and the pure gas-permeation data for all defect-free M3 membranes.

Nonideal permeation effects such as time-dependent membrane aging and bore-fed/shell-fed differences did *not* significantly alter the permeation data, as shown in Table VIII. Sample modules were retested after 1 month and displayed less than a 10% decline in permeance with minimal change in selectivity. There was also less than a 10% decrease in the permeance of shell-fed modules as opposed to a standard bore-fed configuration.

Artifacts within the SEM images were seen to be negligible. The hollow-fiber cross sections were examined at points around the entire circumference to eliminate possible concerns dealing with the cryofracturing technique. The dense skin-layer morphology and thickness did not systematically vary depending on the location on the cross section's circumference. The sputter-coating process had a negligible effect on the cross-sectional morphology as well. Sputtering a gold/palladium alloy created 10-nm bump features across the morphology, which are considered to be the characteristic grain size of the alloy.[46] The 10-nm grain size of the gold/palladium layer should *not* be confused with the 50–200-nm nodule feature size of the membrane. If concerned with these artifacts, a more uniform conductive layer can be applied to the sample's surface by sputter coating with elemental chromium. The chromium layer had a negligible grain size and allowed for a slightly higher resolution in the SEM images. The two sputter-coating processes are compared in Figure 7.

Defective membrane characterization

Ideally, the observation of well-defined apparent defect-free structures, such as those seen in Figure 4b, would be sufficient to guarantee that a defect-free skin has been formed. Nevertheless, we felt it necessary to better test this assumption, since experience has shown that poor performance can sometimes accompany skin and support morphologies that appear "almost perfect." Many articles included in Tables I and II have shown a few SEMs to support theoretical modeling conclusions about membrane morphology, and the preceding results seem to validate this procedure. However, the following section clearly shows the need for caution with regard to the use of SEM analysis and

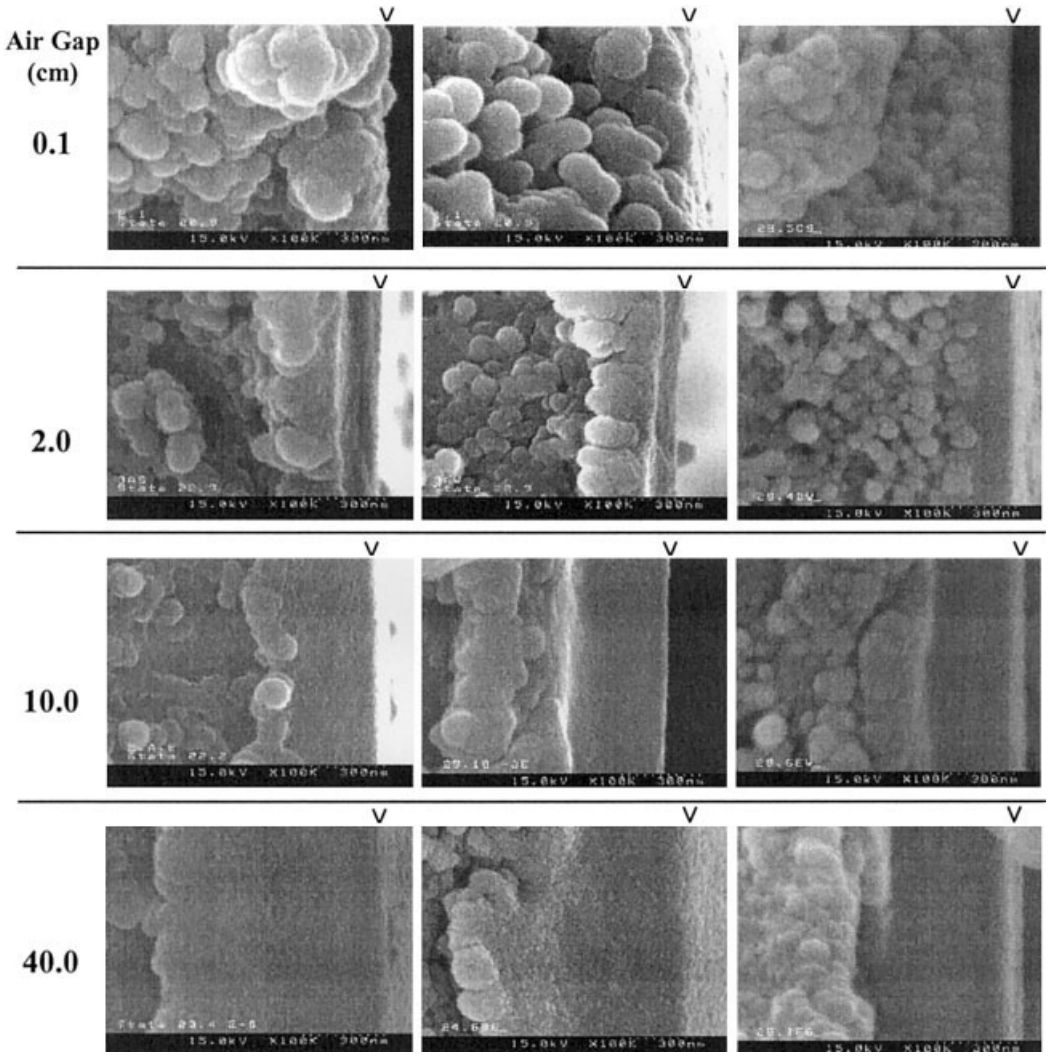

Figure 5 Typical skin layer SEM images from crosssections of hollow fibers formed at various air-gap distances. The skin layer is vertically aligned and the edge of the cross section is denoted by a v. × 100k.

that such analysis is a necessary but not sufficient criterion to apply in understanding the detailed morphologies of these complex structures. To characterize the transition from a truly defect-free morphology to an obviously defective one, three sets of defective versions of the M3 control fibers were formed having well-characterized gas-permeation properties that would be considered "suboptimal or worthless." The gas-permeation data and SEM images are summarized in Table IX and Figure 8.

Severely defective membranes (M3-25)

The first set of fibers was spun from an M3 dope using an ambient spinning temperature of 25°C, as opposed to the standard 50°C. This new set of fibers was labeled M3-25 and was formed using air-gap distances of 0.1, 2, 10, and 40 cm with an air-gap humidity of 67% RH. The M3-25 fibers were *severely* defective for all air gap distances as characterized by gas-permeation measurements *and* SEM images. The fibers displayed essentially Knudsen gas selectivities, and gas permeances were three orders of magnitude higher than that of the control-case fibers formed with a spinning temperature of 50°C. SEM images of the outer-skin region showed a well-developed nodular morphology with an indiscernible difference for all air-gap distances, as shown in Figure 8(a–d). The dense skin layer morphology was *not* seen in the fibers and there was minimal asymmetry near the skin region. Detailed analysis of the causes of the marked differences in performance due to the difference in spinning temperature can involve coupled thermodynamic as well as mass-transfer issues. For the present purposes, these detailed causes are not the point of interest here, but, rather, that SEM analysis and the as-permeation measurements agreed that a selective skin layer was not present.

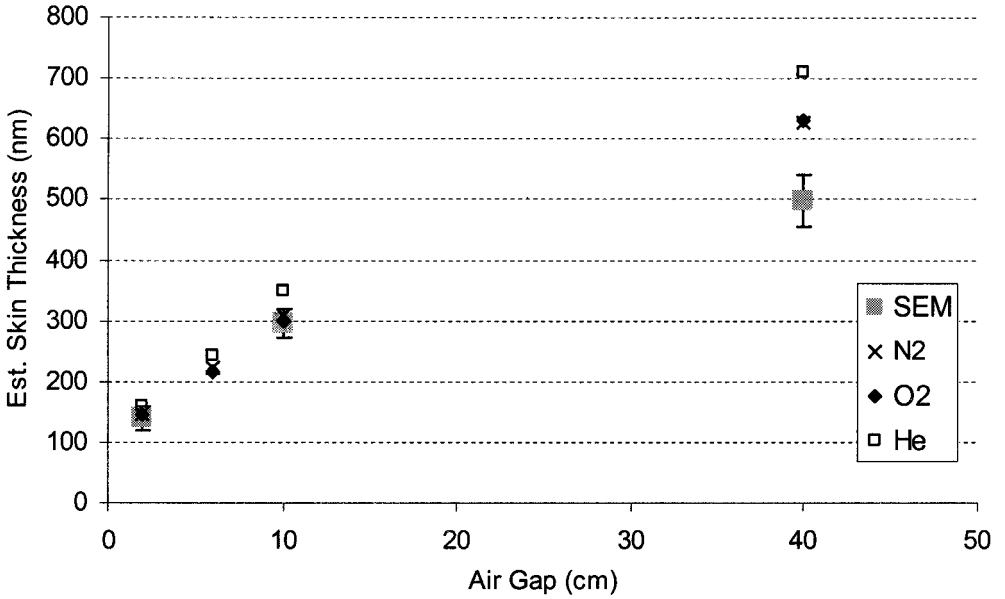

Figure 6 Estimated defect-free skin thickness from SEM images and pure gas N_2, O_2, and He permeation measurements from M3 hollow fibers. Each SEM value represents 36 measurements over three cross sections. Duplicate modules represented in Table III were averaged for each of the three gases; 95% confidence intervals are shown for SEM data.

Moderately defective membranes (M3-X)

A second set of defective fibers, M3-X, was formed from an M3 dope that was exposed to high temperatures over 100°C overnight. There was minimal mass loss from the dope, the rheological properties seemed similar to the standard M3 dope, and the fibers were formed under the standard spinning conditions listed in Table V. However, the resulting M3-X fibers displayed gas selectivities of only 55% of dense film values. Pure gas permeances were similar to those formed from the standard M3 dope. SEM images showed that the skin region was noticeably denser than was the underlying substructure; however, the defect-free skin morphology could *not* be seen in these fibers. The outer skin layer could be described as compacted or partially developed nodules, as seen in Figure 8(e–f). In this particular case, an extremely subtle change in dope rheology is believed to have occurred. Earlier, it was noticed that excessive storage at elevated temperatures could cause undesirable spinning results, but it was not known that even 8-h storage at 100°C (versus <1–2-h maximum exposure to temperatures above 90°C) would cause apparent performance losses and visibly different morphologies as seen by SEM. The M3 fiber state clearly reveals that even short excursions in proper storage prior to use can degrade the gas-separation performance achievable with fibers prepared from a properly formulated dope. Although the fundamental cause of this transport performance loss is unclear and not within the scope of this work, the results show that with adequate SEM characterization deviations can certainly be seen from the idealized dense film properties of the M3 control fibers. This can ultimately be used for a form of "combinatorial" screening of different processing, dope handling, and postformation parameters to identify suspicious deviations from a desired defect-free membrane morphology.

TABLE VII
Defect-free Skin-thickness Estimates from SEM Images and Pure Gas N_2, O_2, and He Permeation Measurements from M3 Hollow Fibers

Air gap (cm)	Skin-thickness estimates (nm)	
	SEM	N_2, O_2, He
0.1	NA	NA
2	139 ± 19	152 ± 13
10	295 ± 24	318 ± 18
40	498 ± 43	657 ± 52

Thirty-six SEM measurements over three cross sections were taken for each air-gap distance. Permeation estimates represent the average from all three gases and multiple modules; 95% confidence intervals are shown.

TABLE VIII
Nonideal Permeation Effects: Percent Change of Permeation Data after 1 month and for Shell-fed Configuration as Compared to Bore-fed M3 Hollow Fibers

% Change	Selectivity		Permeance (GPU)		
	O_2/N_2	He/N_2	N_2	O_2	He
After 1 month	−2.4	2.1	−6.6	−8.8	−4.7
Shell-fed versus bore-fed	−2.5	1.4	−5.7	−8.1	−4.5

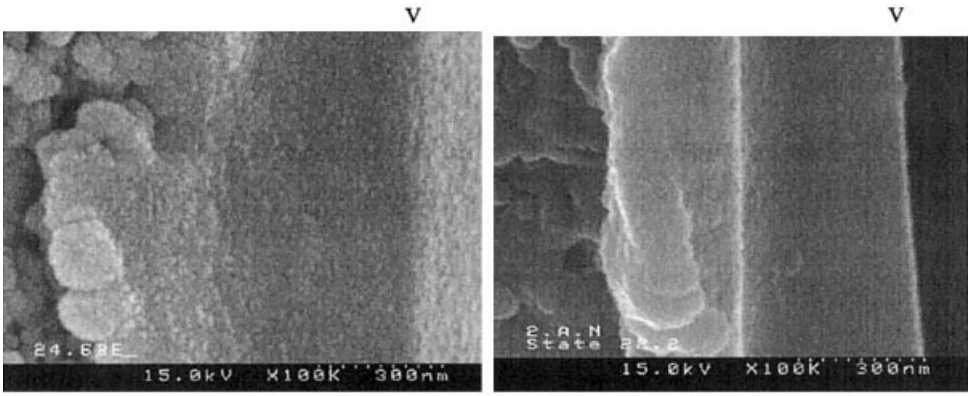

Figure 7 Samples sputter-coated with gold/palladium alloy versus elemental chromium. The small 10-nm bump features present in the Au/Pd sample are attributed to sputtering grain size and not the membrane's morphology. The edge of the cross section is denoted with a v. × 100k.

Slightly defective membranes (M1)

A third set of defective, yet more gas-selective, fibers were formed from a previously described Matrimid® M1 dope.[8] This case is included to illustrate the limitations associated with SEM studies reaching definite conclusions. The M1 dope has less volatile components yet unchanged polymer, solvent, and nonsolvent concentrations. The volatile THF solvent present in the standard M3 dope was replaced with the nonvolatile NMP solvent as shown in Table X. Thus, the only remaining dope component with appreciable volatility is EtOH. Prior work has shown that the subtle changes in dope composition yield less gas-selective membranes than does the M3 control dope.[8] The objective in the present work was to determine whether the resultant morphology as characterized by SEM could actually provide clues as to why the performance of the M1 dope fell below that of the M3 case. The M1 dope was spun into hollow fibers using the standard formation conditions and the resulting fibers exhibited gas selectivities between 70 and 84% of dense film values. While these fibers are considered defective, the overall gas permeances resembled that of the defect-free M3 fibers. Surprisingly, SEM images also showed a dense skin layer morphology analogous to that seen in *defect-free* membranes. Dense layer thicknesses were comparable to the M3 fibers, although a quantitative comparison between SEM images and gas-permeation measurements is *not* considered valid for these defective fibers.

The results from the hollow-fiber membranes with varying degrees of defective gas selectivities somewhat clarify the relationship between the skin morphology and the gas-permeation properties of the hol-

TABLE IX
Pure Gas-permeation Measurements on *Defective* Fibers at Various Air-gap Distances

State	Air gap (cm)	Selectivity		Permeance (GPU)		
		O_2/N_2	He/N_2	N_2	O_2	He
M3-control	10	7.3	103	0.61	4.5	62
M3-25	0.1	0.92	1.9	1750	1611	3313
(Knudsen selectivity)	2	0.95	2.1	122	115	255
				3	9	2
	10	0.95	1.7	332	318	557
				7	0	0
	40	0.93	1.7	375	347	629
				7	9	2
M3-X	6	3.1	34	2.4	7.6	82
(≤55% dense film)	10	3.9	45	1.5	5.7	65
M1	10	6.1	76	0.87	5.3	67
(≤85% dense film)	20	5.6	66	0.86	4.9	58

In relation to the M3 control state, M3-25 fibers were spun at 25°C, M3-X fibers were formed from an annealed dope, and M1 fibers were formed from a dope with less volatile components.

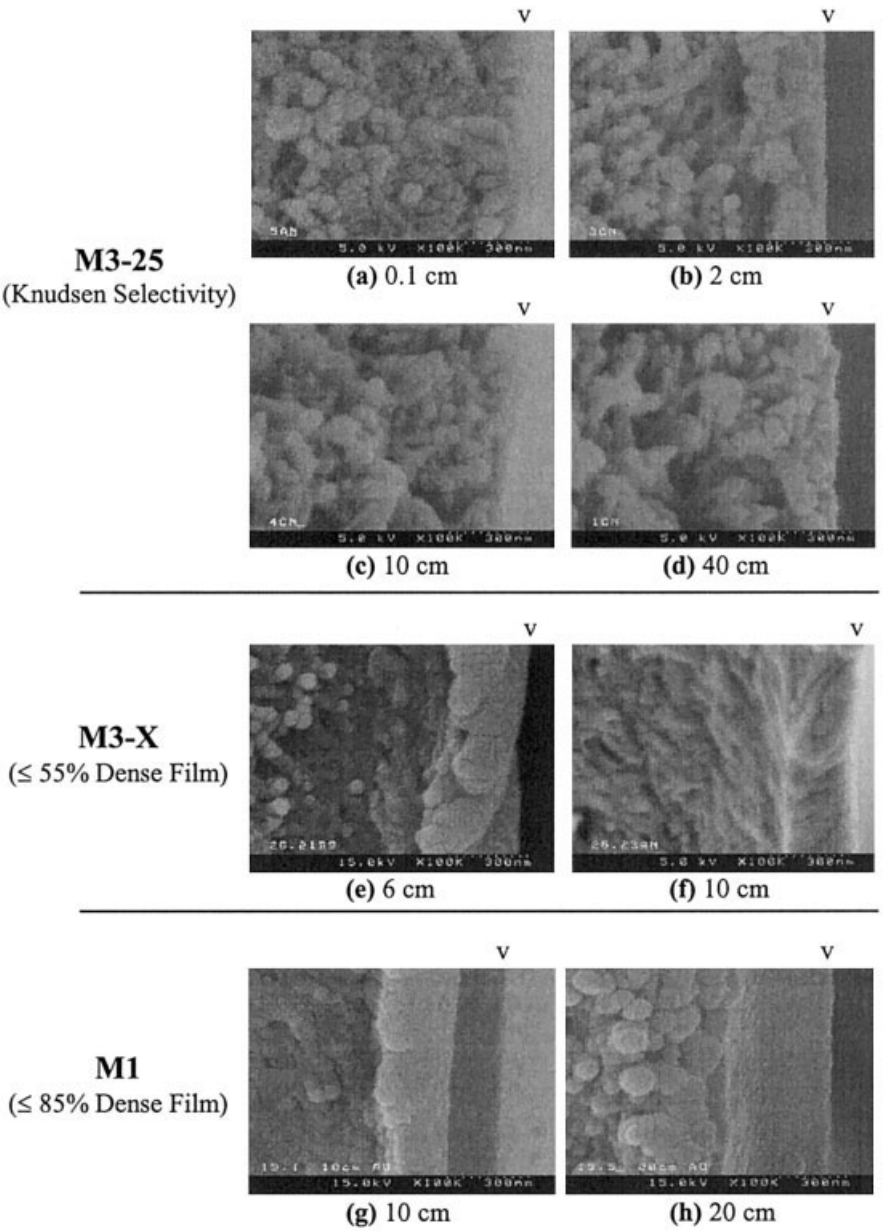

Figure 8 SEM images of *defective* fibers formed at various air gaps from M3-25, M3-X, and M1 hollow-fiber states. v denotes the outer surface of fiber. × 100k.

low-fiber membranes. Severely defective fibers, such as the M1 set and the M3 fibers spun at a 0.1-cm air gap, displayed symmetric well-defined nodular skin morphologies with minimal compaction. With the complementary gas-permeation results, one can use SEM analysis as a detective tool to identify likely morphologies (nodular skins) that will tend to lead to some degree of defective performance. The preceding cases show, however, that the degree of defectiveness between different nodular morphologies is virtually impossible to quantitatively evaluate except by gas probes. Less defective fibers, such as the M3-X and M1 sets, displayed asymmetric morphologies with skin layers of either partially developed nodules or a dense uniform layer. As the gas selectivity of the membranes increased, nodule formation in the skin layer was seen to decrease, leading to a denser morphology and, ultimately, to an apparently defect-free skin layer. Although these results show that SEM images can help

TABLE X
Dope "M1" Composition

Dope ("M1")	
Matrimid®	26.2% wt
NMP	58.9
THF	
EtOH (mixed~24 h ≤40°C)	14.9

guide the visualization of actual morphology changes achieved by systematic dope optimization studies, SEM analysis must remain only a supporting method to gas-permeation measurements. Nevertheless, SEM images may allow for a quick *qualitative* estimate of skin formation propensity to understand when spinning conditions are "almost" at the desirable point of intrinsically defect-free properties.

CONCLUSIONS

A morphologically unique dense skin layer was able to be seen in all defect-free membranes and even slightly defective membranes. For more defective membranes, the presence and extent of nodules in the skin layer increased. Presumably, less-than-perfect internodular fusion causes the apparent defects in the nodular-type skin layers. This set of data gives a strong *qualitative* link between the skin morphology and gas-permeation properties. This also suggests that the suppression of nodule formation in the skin layer could lead to defect-free membrane formation.

For the defect-free hollow-fiber membranes, a semi-*quantitative* agreement was found between the dense skin thickness observed from SEM images and that estimated from pure gas permeances. Thus, the dense skin layer is seen as the sole selective entity of the membrane. SEM images of thick-skinned membranes underestimated skin thicknesses based on gas permeation, although this could be due to substructure resistance or the ambiguous morphology of the substructure. Minimal effects were seen from membrane aging, shell/bore-fed configurations, and SEM artifacts from the sputter-coating process.

It is important to note that a standard 70-cm^2 lab-scale hollow-fiber module is capable of characterizing a few *billion* times the amount of the active membrane area as one high-resolution SEM. Although SEM images provide a powerful supporting characterization technique, they cannot substitute for analytical gas-permeation measurements. Rather, this SEM analysis was intended to provide firm experimental support that defect-free membranes indeed have a unique gas-selective entity with a distinctly dense morphology—in other words, to show that the elusive defect-free skin morphology *"exists"* true to its visualization. This represents the first time such an in-depth analysis of the defect-free morphology has been performed. Used together, SEM coupled with a systematic spinning and permeation testing program provides a highly efficient way to optimize practical conditions and solution formulations to produce a truly dense and defect-free membrane structure.

The authors gratefully acknowledge the support of this research by Air Liquide and the helpful loan of the high-performance spinneret used in this work to allow investigating the influence of morphology using realistic preparation conditions and spinning hardware.

References

1. Henis, J. M. S.; Tripodi, M. K. J Membr Sci 1981, 8, 233.
2. Koros, W. J.; Fleming, G. K. J Membr Sci 1993, 83, 1–80.
3. Pinnau, I.; Koros, W. J. J Membr Sci 1993, 71, 81.
4. Kesting, R. E.; Fritzsche, A. K. Polymeric Gas Separation Membranes; Wiley: New York, 1993.
5. Kesting, R. E. Synthetic Polymeric Membranes: A Structural Perspective, 2nd ed.; Wiley: New York, 1985.
6. Mulder, M. Basic Principles of Membrane Technology; Kluwer: Dordrecht, 1996.
7. Pinnau, I.; Freeman, B. D., Membrane Formation and Modification; Eds.; American Chemical Society, Washington, DC, 2000; Vol. 744.
8. Clausi, D. T.; Koros, W. J. J Membr Sci 2000, 167, 79.
9. Clausi, D. T. Ph.D. Dissertation, The University of Texas at Austin, 1998.
10. Kawakami, H.; Nagaoka, S. In Membrane Formation and Modification; Pinnau, I.; Freeman, B. D., Eds.; American Chemical Society: Washington, DC, 2000, Vol. 744, p 79.
11. Kim, H. J.; Tabe-Mohammadi, A.; Kumar, A.; Fouda, A. E. J Membr Sci 1999, 161, 229.
12. Kawakami, H.; Mikawa, M.; Nagaoka, S. J Membr Sci 1997, 137, 241.
13. Pesek, S. C.; Koros, W. J. J Membr Sci 1993, 81, 71.
14. Pinnau, I.; Koros, W. J. J Appl Polym Sci 1992, 46, 1195.
15. van't Hof, J. A.; Reuvers, A. J.; Boom, R. M.; Rolevink, H. H. M.; Smolders, C. A. J Membr Sci 1992, 70, 17.
16. Pinnau, I.; Koros, W. J. J Appl Polym Sci 1991, 43, 1491.
17. Pinnau, I.; Koros, W. J. Membr Sci 1992, 71, 81.
18. Fritzsche, A. K.; Murphy, M. K.; Cruse, C. A.; Malon, R. F.; Kesting, R. E. Gas Sep Purif 1989, 3, 106.
19. Kawakami, H.; Mikawa, M.; Nagaoka, S. Macromolecules 1998, 31, 6636.
20. Pinnau, I.; Koros, W. J. J Polym Sci Part B Polym Phys 1996, 31, 419.
21. Wienk, I. M.; Boom, R.; Beerlage, M.; Butte, A.; Smolders, C.; Strathemann, H. J. Membr. Sci. 1996, 113, 361.
22. Wang, D.; Li, K.; Teo, T. K. J Membr Sci 2000, 176, 147.
23. Chung, T.-S.; Lin, W.-H.; Vora, R. H. J Membr Sci 2000, 167, 55.
24. Chung, T.-S.; Shieh, J.-J.; Lau, W. W. Y.; Srinivasan, M. P.; Paul, D. R. J Membr Sci 1999, 152, 211.
25. Wang, D.; Li, K.; Teo, W. K. J Membr Sci 1998, 138, 193.
26. Wang, D.; Li, K.; Teo, W. K. J Membr Sci 1996, 115, 85.
27. Ekiner, O. M.; Vassilatos, G. J Membr Sci 1990, 53, 259.
28. Ekiner, O. M.; Vassilatos, G. U.S. Patent 5,085,774; DuPont, 1992.
29. Fritzsche, A. K.; Cruse, C. A.; Murphy, M. K.; Kesting, R. E. J Membr Sci 1990, 54, 29.
30. Fritzsche, A. K.; Cruse, C. A.; Kesting, R. E.; Murphy, M. K. J Appl Polym Sci 1990, 40, 19.
31. Fritzsche, A. K.; Armbruster, B. L.; Fraundorf, P. B.; Pellegrin, C. J. J Appl Polym Sci 1990, 39, 1915.
32. Fritzsche, A. K.; Cruse, C. A.; Kesting, R. E.; Murphy, M. K. J Appl Polym Sci 1990, 41, 713.
33. Kesting, R. E.; Fritzsche, A. K.; Cruse, C. A.; Moore, M. D. J Appl Polym Sci 1990, 40, 1575.
34. Cabasso, I.; Robert, K. Q.; Klein, E.; Smith, J. K. J Appl Polym Sci 1977, 21, 1883.

35. Cabasso, I.; Klein, E.; Smith, J. K. J Appl Polym Sci 1976, 20, 2377.
36. Niwa, M.; Kawakami, H.; Nagaoka, S.; Kanamori, T.; Shinbo, T. J Membr Sci 2000, 171, 253.
37. Li, S. G.; Koops, G. H.; Mulder, M. H. V.; Boomgard, T. v. d.; Smolders, C. A. J Membr Sci 1994, 94, 329.
38. Pesek, S. J Membr Sci 1994, 88, 1.
39. Chung, T. S.; Kafchinski, E. R.; Vora, R. J Membr Sci 1994, 88, 21.
40. McKelvey, S. A.; Clausi, D. T.; Koros, W. J. J Membr Sci 1997, 124, 223.
41. Ekiner, O. M.; Hayes, R. A. U.S. Patent 4,983,191, DuPont, 1991.
42. Ciba Specialty Chemicals, 1998.
43. Burdick & Jackson Solvent Guide; Allied Signal, 1997.
44. Pesek, S. C.; Ph.D. Dissertation, The University of Texas at Austin, 1993.
45. Box, G.; Hunter, W.; Hunter, J. Statistics for Experimenters; New York, 1978.
46. Sawyer, L. C.; Grubb, D. T. Polymer Microscopy, Chapman & Hall: New York, 1996.